

WAVELET ANALYSIS OF THE POTENTIAL FIELDS OF ELASTICITY: A REMOTE SENSING TOOL TO MONITOR STEAM CAP MIGRATIONS?

Franklin G. Horowitz^{1,2}, Peter Hornby², Eric J. Fielding³, Klaus Regenauer-Lieb^{1,4}

¹Western Australia Geothermal Centre of Excellence

²CSIRO Exploration and Mining

³Jet Propulsion Laboratory, Caltech, Pasadena, CA, USA

⁴School of Earth and Environment, The University of Western Australia

c/o CSIRO/ARRC, 26 Dick Perry Ave.

Kensington, W.A., 6151, Australia

e-mail: frank.horowitz@csiro.au

ABSTRACT

A technology based upon analyses of InSAR surveys of incremental deformations over an operating geothermal field is emerging that might serve to monitor steam cap migrations on a timescale of weeks. Based upon theory developed in Horowitz and Hornby (in prep.), one can compute a harmonic potential field that has dilatational sources and sinks from 3 component surface displacement increment surveys. In the context of a water-steam fluid in porous rocks, steam filled material will have significantly different bulk moduli from water-filled material. In the presence of a regional stress field, changes in the pore-filling will appear as dilatational sources or sinks. There are commercial InSAR satellites in operation (e.g. Canada's Radarsat-1 and Radarsat-2), and a research system (ALOS PALSAR from Japan) is in orbit with L-band capabilities that can penetrate vegetation canopies. Imaging geometries may be problematic for computing three component displacement surveys over any given area, but we have successfully solved for the 3-component field in the case of afterslip from the 2003 Bam, Iran earthquake. We believe that this technology might be a cost-effective and higher sampling rate alternative/supplement to microgravity surveying for monitoring the migration of steam caps in an operating geothermal field.

INTRODUCTION

Steam cap migration in certain types of geothermal fields is of major concern -- perhaps even requiring changes in the method of those fields' operation. Thus, monitoring steam cap migration is necessary. Physically, steam cap motions change two things that are potentially observable from surface displacement-field measurements. First, in (e.g.) an undrained fracture, they can cause direct inflation of the

surrounding rocks. Second, the partial change of state of the pore fluid from liquid to gas causes a change in the effective bulk modulus of the rock-pore-fluid system. In the presence of a confining pressure or a regional stress field this bulk modulus change can appear as a location of effective contraction or expansion -- i.e. a negative or positive dilatation. From linear elasticity, we know that the magnitude of the far-field incremental deformations on the ground surface due to such changes is proportional to the new volume produced or consumed (e.g. Lecampion et al., 2005).

Interferometric Synthetic Aperture Radar (InSAR) is a well-known satellite based technique that can measure surface deformation increments (e.g. Bürgmann et al., 2000). A pair of scenes from the same satellite acquired at times t_0 and t_1 can be processed to yield range changes -- or incremental displacements projected onto the line-of-sight vector -- between the satellite and the pixel on the ground. InSAR satellites are in near-polar orbits. These orbital geometries are problematic for acquiring the 3 non-coplanar range changes required for the technique described below. One of the goals of this work is to determine how much of a problem the acquisition geometries would be in practice. The effect of the level of measurement noise found in InSAR observations is also important to quantify.

Under certain approximations applicable here (Horowitz and Hornby, in prep.) there is an exact mathematical analog between elasticity solutions for these free surface problems and harmonic potential fields. Moreover, we can actually compute harmonic potential fields on the free surface from 3 component displacement increment measurements. This means that we can interpret these measurements in a very similar manner to measurements from gravity or magnetic surveys, rather than needing to resort to inverse problems to describe the underground sources. In particular, we can analyze the results using the wavelet specifically tuned to the physics of potential fields described by Moreau et al. (1997)

(independently derived by Hornby et al., 1999) and widely deployed in the mineral exploration industry. The key difference here is that our underground sources are not mass-density or magnetic susceptibility contrasts, but rather are nuclei of dilatational or rotational deformations.

From potential theory, we know that the magnitude of the surface displacements should be inversely proportional to the first or second power of the depth of the source -- depending upon geometry of the source. Combining this effect with the crack volume argument above, this argues for a competition between size, nature, and depth of the source that leaves us unsure about the expected magnitude of the deformation signal at the surface. We resort to numerical simulation of some crude, but hopefully representative deformations in order to predict the kind of signal that might be measurable at the surface.

Our hypothesis then, is that steam cap migrations in geothermal fields cause surface deformations of sufficient amplitude both to be monitored by satellite based InSAR measurements, and to be interpretable as elastic potential fields using wavelets.

METHODS

Finite element simulations

Using the commercial Finite Element Method (FEM) package Abaqus/CAE, meshes were constructed for a 10 cm thick disk of various radii, orientations, and burial depths. Although we thought of it as being empty, to satisfy the meshing requirements of Abaqus the interior of the disk was made elastic with a very compliant Young's Modulus of 0.1 MPa and a Poisson's ratio of 0.25. The disk was embedded in a linear elastic block of $2\text{km} \times 2\text{km} \times 1\text{km}$ depth, with Young's Modulus 40 GPa, and Poisson's ratio 0.25. Figure 1 shows a horizontal 250m radius disk buried at 250m depth.

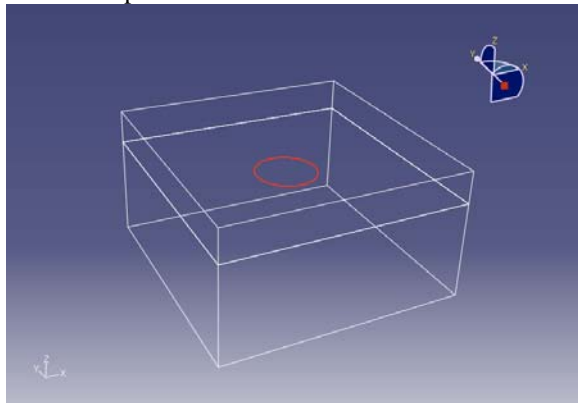


Figure 1: Geometry of a 10cm thick, 250m-radius horizontal disk buried at 250m depth. In all the following figures, X is positive to the East, Y is positive to the North, and Z is positive up.

The mesh corresponding to Fig. 1 is shown in Figure 2. It consists of some 26,400 “hybrid” quadratic hexahedral elements allowing for a linear variation in pressure within the interior of each element. There is a layer of 10cm thick elements at the depth of the disk, again to satisfy Abaqus meshing requirements.

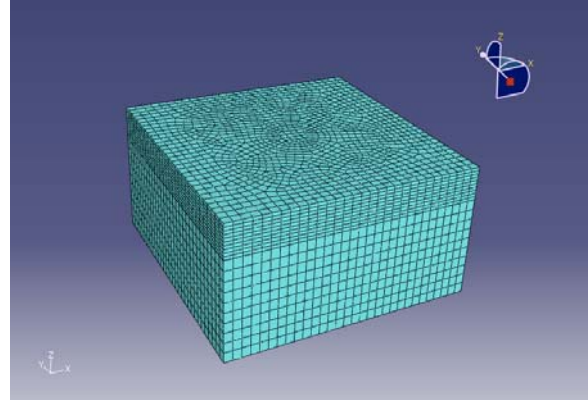


Figure 2: the FEM mesh for a horizontal 250m radius disk.

Boundary conditions and loads were specified appropriately for a linear perturbation analysis simulating inflation of the disk. The bottom southwestern-most corner was fixed – i.e. not allowed to displace or rotate in any degree of freedom. The bottom southeastern-most corner was not allowed to displace in the Y direction or to rotate about the X or Z axes. Similarly, the bottom northwestern-most corner was not allowed to displace in the X direction or to rotate about the Y or Z axes. All nodes in the lowermost boundary were not allowed to displace in the Z direction. The top boundary is a free surface. The interior faces of the crack were loaded with a pressure of 2.5 MPa, the hydrostatic pressure of water at that depth – chosen to be representative of the magnitude of steam-flash overpressure. From the steam tables, this corresponds to $\sim 225^\circ\text{C}$ water flashing to steam.

The resulting displacement field on the surface of the disk is shown in Figure 3, and the free-surface displacement field on the top boundary is shown in Figure 4.

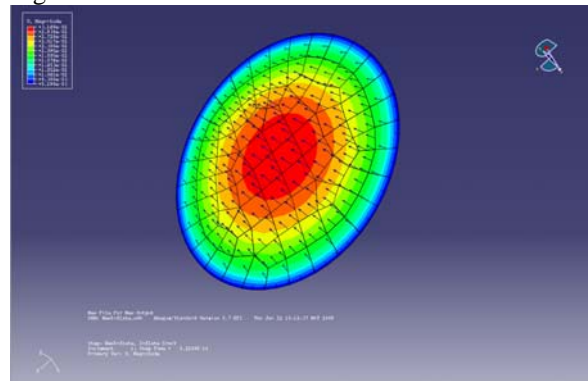


Figure 3: Displacement field (and mesh) on the

upper surface of the disk (in the interior of the elastic block) due to the inflation problem described above. Colors indicate the magnitude of displacement (peak $\sim 32\text{mm}$) and the vector field is displayed with lengths proportional to the magnitudes.

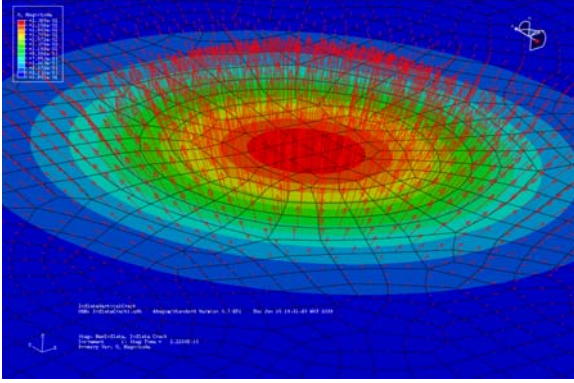


Figure 4: Close-up of the free-surface displacement field. Peak displacements are about 22mm. The strong divergence of the field is apparent from the changes in vector directions from one side to the other.

Interpolation to a Regular Grid

The FEM program reports the free-surface displacement field only at the positions of the nodes. Our potential fields processing requires data on a regular grid. To change from the irregular nodal sampling to a regular grid, each vector component of the displacement field was separately interpolated to a 256×256 pixel grid using a thin-plate spline radial basis function (RBF) interpolation.

Fourier Domain Processing

Each resulting field was then embedded into a 512×512 grid allowing for a spatial Hann (“cosine bell”) filter around the exterior of the interpolated field. This is a standard technique to reduce Fourier domain artifacts due to the sharp edges of our 256×256 region of interest and the periodic “wrap around” boundary conditions imposed by Fast (Direct) Fourier Transform processing.

Horizontal gradients are calculated using the Fourier representation of a central (finite) difference operator for both the X and Y directions.

Elasticity and Connections to Potential Fields

Horowitz and Hornby (in prep.) show that if u is the vector field, its divergence $\nabla \cdot u$ is harmonic. That is, divergence of the displacement field obeys Laplace’s equation $\nabla^2(\nabla \cdot u) = 0$ for these elasticity problems. When the right-hand side of Laplace’s equation is non-zero, it becomes Poisson’s equation, which represents the response to underground sources.

Poisson’s equation is identical in form to the governing equation for gravity surveys, where sources are mass-density contrasts. Here, sources are nuclei of dilatation.

Horowitz and Hornby (in prep.) further show that on the free surface, due to the boundary condition, the 3D $\nabla \cdot u$ can be estimated directly from observed quantities without needing a vertical gradient. That is, $[\nabla \cdot u]_{z=0} = (\partial u_1 / \partial x + \partial u_2 / \partial y)_{z=0}$ where $z = 0$ is the free surface.

In essence, this means that we can compute a harmonic function derived from quantities that we observe with InSAR.

The implication is that our derived harmonic quantity may now be subject to all of the usual operations permissible for a potential field, including computation of vertical gradients, upward continuation, and the calculation of potential field wavelets and their multi-scale edges (“worms”) according to the techniques of Hornby et al. (1999). In this context, “upward continuation” and other such operations above the free surface refer to taking the traction-free deformation at the free surface and notionally inserting it into an elastic whole-space. The divergence of the resulting deformation in the elastic body above the $z = 0$ plane then is treated much like the upward continuation of (e.g.) the gravitational field in a traditional potential field analysis. Such operations are most conveniently performed in the Fourier domain.

For completeness, we briefly mention that there is another such harmonic quantity derivable from InSAR observations: the vertical component of the curl of u ($\nabla \times u$). Given that sources for this harmonic function are nuclei of rotation (as opposed to nuclei of dilatation for $\nabla \cdot u$) and that such sources are likely of less interest in the context of a geothermal field, for the rest of this paper we do not concentrate on analyzing $\nabla \times u$.

Observational Geometry

Satellite based InSAR systems do not observe directly the 3 Cartesian components of the displacement-increment field. Rather, for our purposes, a single time t_0 through to time t_1 interferometric scene-pair observes distance changes along the line-of-sight from the satellite to the ground pixel. This means we observe a single component of the incremental displacement (from t_0 to t_1) with each scene-pair. To estimate the full 3 components of the displacement increment vector, we need 3 lines-of-sight that are not co-planar (in order to “span” the 3D vector space of the displacement increments).

Subject to operational constraints, polar orbiting InSAR satellites can observe the same patch of ground during either the “ascending” (i.e. a northward crossing of the equator) or “descending” portions of their orbits. Denote the ascending and

descending line-of-sight unit vectors by b_a and b_d respectively.

For current InSAR satellite systems, our operational problem becomes finding some “other” nearby orbit that can observe the same patch of ground with a line-of-sight unit vector – denoted b_o . We require b_o to lie far enough out of the plane spanned by b_a and b_d that we can successfully resolve the 3 Cartesian components of the displacement increments, and their horizontal gradients.

Kaiser (1994; pages 15-18) shows a simple method to transform observations from the non-orthonormal line-of-sight basis vectors to the usual orthonormal Cartesian basis. A “metric operator” is formed from the outer products of the line-of-sight vectors:

$$(1) \quad G = (b_a \otimes b_a) + (b_d \otimes b_d) + (b_o \otimes b_o)$$

G is then inverted, and used to calculate the bi-orthogonal reciprocal basis set (superscripts):

$$(2) \quad \{b^a, b^d, b^o\} = G^{-1} \{b_a, b_d, b_o\}$$

Rectification into Cartesian coordinates is finally accomplished by means of multiplying the (scalar) components observed along the lines-of-sight with the corresponding reciprocal basis vectors:

$$(3) \quad u = c_a b^a + c_d b^d + c_o b^o$$

Horowitz and Hornby (2006; using data supplied by one of the present co-authors: Eric Fielding) have previously performed an elastic potential fields InSAR analysis of afterslip from the December 26 2003 Bam, Iran earthquake (Fielding, et al., 2009). Borrowing the observation directions from that analysis, we simulate the InSAR observations of our FEM nodal displacement fields by projecting the Cartesian FEM results onto the lines-of-sight from the Bam work. In this case, b_o lies about 3.1 degrees out of the plane formed by b_a and b_d . We rectify the resulting 3 projections of the FEM displacements back into the original Cartesian frame of reference using equations 1 through 3. We find that the *maximum* error in any component over the whole collection of displacement field vectors is some 5 orders of magnitude lower than the value of that component. Figure 5 shows a perspective and in-plane view of the lines-of-sight.

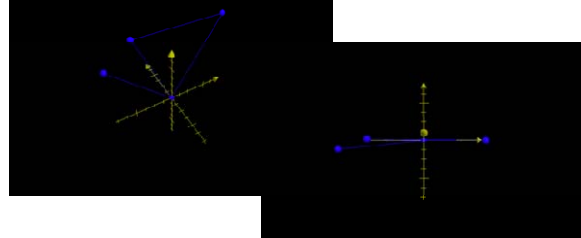


Figure 5: Two views of unit vectors for the observational geometry from the Bam, Iran analysis of Horowitz and Hornby (2006).

The left panel shows a perspective view, with b_a and b_d forming a triangle, and b_o isolated. The yellow arrows are East pointing towards the upper right, North pointing towards the upper left, and Z vertical. The right panel offers a view in the plane of b_a and b_d . The small out-of-plane angle of b_o is shown.

Simulating Observational Noise

Dawson and Tregoning (2007) analyzed the noise found in C-band (5.6 cm wavelength) InSAR observations over Australia, and conclude that a Gaussian distribution with zero mean is a reasonable fit to the error distribution. They report standard deviations “can approach ± 2 mm (1σ) and is routinely at the ± 4 mm level”.

The pixel-to-pixel level of noise for InSAR data is usually taken as a proxy for the interferometric coherence (Fielding et al., 2005). The high levels of noise we use here are for data with little or no smoothing applied. Most InSAR processing includes some spatial smoothing that degrades spatial resolution to mitigate the noise. InSAR at L-band (23.6 cm wavelength for ALOS/PALSAR) can have lower levels of noise than C-band in many areas.

We simulated the effect of InSAR observational noise by drawing random numbers from a zero mean Gaussian distribution of 2 mm standard deviation. These random numbers were then summed as perturbations into the simulated line-of-sight InSAR observations. We then repeated the rectification, computation of $\nabla \cdot u$, and wavelet multi-scale analysis described above with these simulated noisy observations.

RESULTS

Rectification

Table 1 shows the observation lines-of-sight from the Bam example, and their corresponding reciprocal bases. Note that the Y components of the reciprocal basis vectors are much larger than their X or Z components.

Vector	X	Y	Z
b_a	-0.318049	-0.089164	0.920245
b^a	-1.041633	16.052377	2.21069
b_d	0.416705	-0.09743	0.903805
b^d	1.199488	-5.20026	-0.00718
b_o	-0.62840	-0.14600	0.76407
b^o	-0.16431	-13.18224	-1.34529

Table 1: Lines-of-sight vector components (subscripted) and their corresponding bi-

orthogonal reciprocal basis vectors (superscripted). The average Y component of the reciprocal bases is some 11.5 times larger than the average of the combined X and Z components.

Noise Free Analysis

Based upon the deformation displayed in Figs. 3 and 4, Figure 6 shows the FEM free-surface displacement field in a lines-of-sight coordinate basis, interpolated onto a regular grid. Figure 7 shows gradients and the divergence computed from the same vector field after rectification. Figure 8 shows a multi-scale edge (“worm”) analysis of the results.

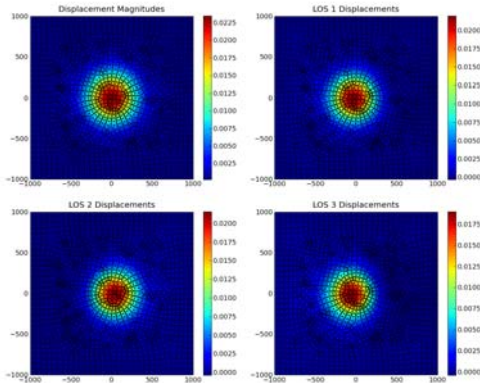


Figure 6: Line of sight observations. The upper left panel shows the “clean” displacement field magnitude at the free surface ($z=0$) from the FEM calculation of Figures 3 and 4. It will be repeated in all following figures of this type for visual reference. The other three panels show the displacement field at $z=0$ projected along the three lines-of-sight described in the Methods section. Observations are collected at the locations of the nodes (small circles) and interpolated onto a regular grid. All units are in meters.

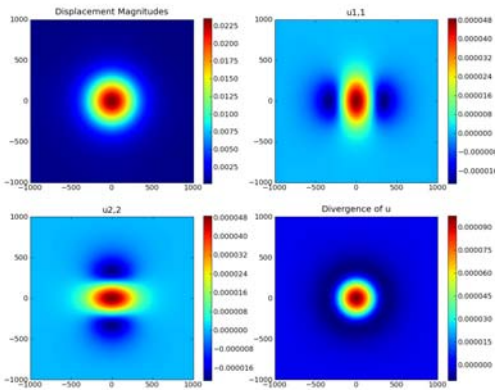


Figure 7: Horizontal gradients, and the resulting divergence on the free surface $z=0$. The data have been rectified from Figure 6. The upper left panel is the same as described in Figure 6. The upper right panel shows $\partial u_1/\partial x$ and the lower left shows $\partial u_2/\partial y$ which are equivalent to the strains ϵ_{11} and ϵ_{22} respectively. The lower right panel shows $\nabla \cdot u$ (equivalent to the trace or first invariant of the strain tensor) as estimated from the 2D free surface computation described in the Methods section. Units for the latter three panels are dimensionless (i.e. meters per meter). Results directly from the FEM calculations that have not suffered the line-of-sight projection and rectification procedure are visually indistinguishable.

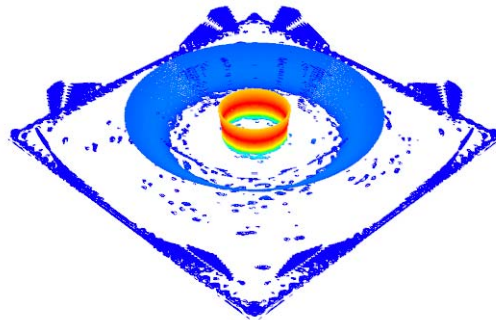


Figure 8: Wavelet multiscale edge “worm” analysis of the divergence field from Figure 7. The theory of these multiscale edges is described in Hornby et al. (1999), where it is shown that upward continuation is essentially a wavelet scale change. Briefly, maxima in horizontal gradients of the underlying harmonic function are marked, and colored proportional to the strength of the gradient. The amplitude behavior with height, the attitude of the “worm sheets”, and the intersections of two “worm sheets” caused by the same underground source distribution all contain interpretable information about the size, attitude, depth, and Lipschitz exponent of the causative source. Worms are particularly useful in interpreting information about multiple regional sources, or those sources with more complicated geometries than the sources studied in this paper.

Small features at the lower levels, and features near the lateral edges of the analysis are both due to different kinds of numerical noise.

Analysis of Data with Simulated InSAR Noise

In these displays, we parallel the results displayed for the noise-free data. Figure 9 shows the simulated InSAR noise projected onto the lines-of-sight. Figure 10 shows the resulting gradients and divergence estimate. Figure 11 shows the resulting worm sheet analysis.

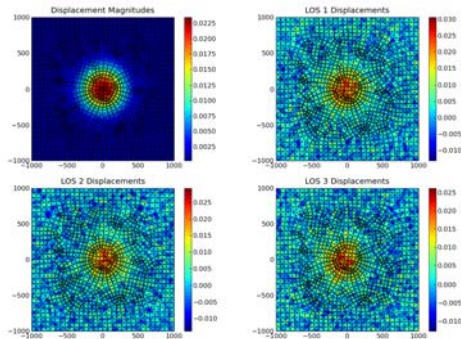


Figure 9: Line of sight observations. These are the analogs of Figure 6 with the simulated noise described in the methods section added to the underlying range-changes.

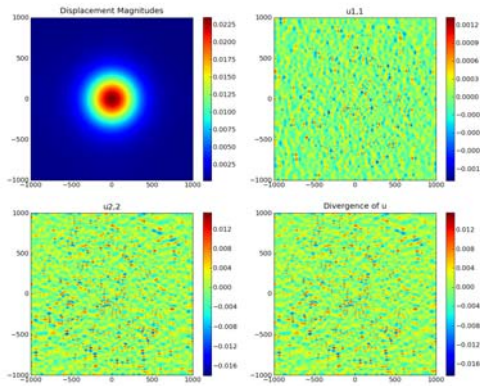


Figure 10: Gradients and divergence on the free surface. These are the noisy analogs of Figure 7.

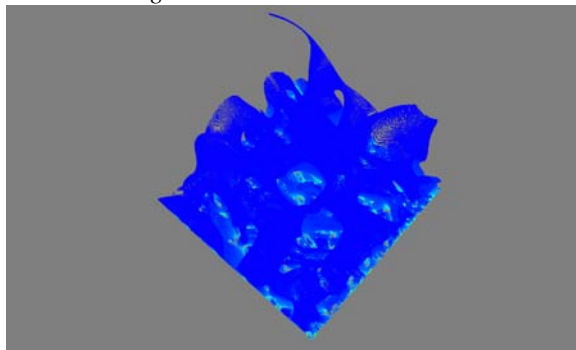


Figure 11: Wavelet multiscale edge “worm” analysis of the divergence field from Figure 10. This is the noisy analog of Figure 8.

Because of the difference between Figures 7 and 10, we also plot the data of Figure 10 upward continued 500 meters. The result of this operation is shown in Figure 12.

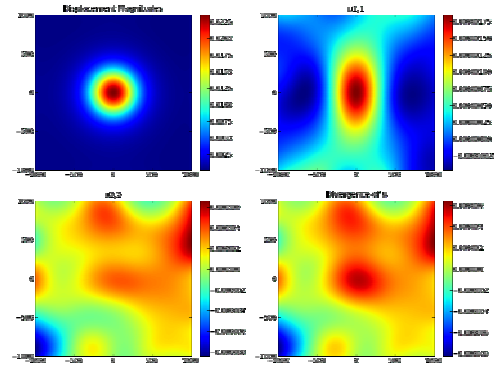


Figure 12: The gradients and divergence of Figure 10 are shown after 500 meters of upward continuation.

DISCUSSION

For the deformation studied, the satellite acquisition geometry used is adequate for noise-free data, but inadequate in the presence of observational noise. This is clearly evident in the difference between Figures 8 and 11. The results in Figure 8 are nearly as good as any results ever produced by the technique of Hornby et al. (1999). In particular, the lateral outlines are nicely delineated, the class of discontinuity would be estimable from the amplitude variations along the cylindrical worm-sheet, and the (extrapolated) intersection of the conical and cylindrical worm sheets contains easily visualized information about the depth of the source. Note that depth estimation is a particularly difficult problem in potential fields, usually requiring a full inverse problem. Here the answer is visual. However, the results of Figure 11 are, to put it bluntly, uninterpretable.

The signal to noise (S/N) ratio on the free surface is strongly anisotropic, due to the acquisition geometry. This can best be seen via considering the magnitude of the reciprocal basis vector components in Table 1. On average, the North-South components are about 11.5 times larger in magnitude than the summed East-West and up-down components. From equation 3 we see this implies the effects of noise in the North-South direction will be magnified 11.5 times more in that direction than in the other directions. Another way of stating the same thing is that the error ellipses on $z = 0$ are strongly stretched in the N-S direction. Because our potential fields computation is based upon numerically computed gradients, the results are sensitive to the amount of noise. Even though the East-West gradients at $z = 0$ shown in Figure 10 are

noise contaminated, the underlying field is still evident after upward continuation. This is clearly demonstrated in the upper right panel of Figure 12, and illustrates one of the strong advantages of using wavelets to analyze noisy data – scale changes average out noise very effectively. Unfortunately, because of the anisotropic S/N, the true North-South gradients are not adequately represented, as shown in the lower left panel of Figure 12.

Even given all of the above issues with noise, the true target is actually visible in Figure 12 – if you know where to look in advance. Of course, the problem in an exploration or monitoring context is that the location of a signal is a large part of what you need to decipher in the first place. Clearly the S/N issues are a distraction from that task.

Because of the competition between the source region's depth and its incremental volume, the amplitude of the free surface displacement field signal (and hence the S/N) is case dependent. Deformations produced by steam cap migrations (or other processes of interest to operating geothermal fields) other than the crude ones simulated by our FEM work may well enjoy better detectability with these methods.

One possible remedy to the problems found here is to fix a drawback in the current theoretical approach. At the moment, we ignore the Z component of the data – which happens to have a high S/N. In the current state of the theory, this would entail decoupling the contributions to u_z of the dilatational part from the rotational part of the field. Currently, we see no observable way to accomplish this decoupling.

A second possible remedy involves stacking multiple time observations in order to average out the noise. This approach has been successful in the work of Fielding et al. (2009, in press). A disadvantage of such an approach is that the time intervals between informative snapshots would increase.

A third possible remedy involves treating the interpolation step as a full fledged inverse problem. This might well lead to better field or gradient estimates, at a slightly higher computational cost.

Ultimately, we may be faced with the reality that satellite-based InSAR may not be able to resolve deformations of interest to geothermal field operations. While the commercial scene acquisition costs are currently attractive relative to (e.g.) a microgravity survey, they will accrue with time. A new possibility is airborne InSAR that has much greater control over the imaging geometry, and will have much higher spatial resolution, which will aid the identification of small features. NASA/JPL has just completed testing of the airborne UAVSAR system (Rosen et al., 2006). Another possibility is that a ground-based, Lidar surveyed, geodetic network could be placed over a field. Such measurements could be treated identically to the InSAR surveys described here. They could also enjoy

a more favorable, controlled geometry of acquisition, the ability to stack information on very short time scales (perhaps even down to seconds), and smaller running costs than repeated commercial InSAR surveys.

REFERENCES

- Bürgmann, R., Rosen, P. A., & Fielding, E. J. (2000). Synthetic aperture radar interferometry to measure Earth's surface topography and its deformation. *Annual Review of Earth and Planetary Sciences*, **28** (1), 169-209.
- Dawson, J., & Tregoning, P. (2007). Uncertainty analysis of earthquake source parameters determined from InSAR: A simulation study. *Journal of Geophysical Research*, **112** (B9), B09406.
- Fielding, E. J., Talebian, M., Rosen, P. A., Nazari, H., Jackson, J. A., Ghorashi, M., & Walker, R. (2005). Surface ruptures and building damage of the 2003 Bam, Iran, earthquake mapped by satellite synthetic aperture radar interferometric correlation. *Journal of Geophysical Research*, **110**, B03302.
- Fielding, E. J., Lundgren, P. R., Bürgmann, R., & Funning, G. J. (2009). Shallow fault-zone dilatancy recovery after the 2003 Bam, Iran earthquake. *Nature* (in press).
- Hornby, P., Boschetti, F., & Horowitz, F. G. (1999). Analysis of potential field data in the wavelet domain. *Geophysical Journal International*, **137** (1), 175-196.
- Horowitz, F. G., & Hornby, P. (2006). Exploring for the sources of internal elastic deformations using potential fields and their Poisson wavelets; possible applications to InSAR observations. *Eos Transactions AGU*, **87** (52), Fall Meeting Supplement, Abstract G33A-0038.
- Horowitz, F. G., & Hornby, P. (in prep.). Exploring for the nuclei of elastic strain using potential fields and their Poisson wavelets.
- Kaiser, G. (1994). *A Friendly Guide to Wavelets*. 300pp. Boston: Birkhäuser.
- Lecampion, B., Jeffrey, R., & Detournay, E. (2005). Resolving the geometry of hydraulic fractures from tilt measurements. *Pure and Applied Geophysics*, **162** (12), 2433-2452.
- Moreau, F., Gibert, D., Holschneider, M., & Saracco, G. (1997). Wavelet Analysis of Potential Fields. *Inverse Problems*, **13**, 165-178.
- Rosen, P. A., Hensley, S., Wheeler, K., Sadowy, G., Miller, T., Shaffer, S., Muellerschoen, R., Jones, C., Zebker, H., & Madsen, S. (2006). UAVSAR: a new NASA airborne SAR system for science

and technology research. In *Radar, 2006 IEEE Conference on*, (pp. 8 pp.+).

ACKNOWLEDGMENTS

We thank Prof. Arcady Dyskin of UWA for suggesting that treating the gradient estimation (or indeed, the interpolation itself) as a full fledged inverse problem may well bear fruit in solving this problem. We also thank Prof. Boris Gurevich of Curtin University for suggesting the inflationary loading as an alternative to simple bulk modulus changes. Finally, we thank Thomas Poulet for numerous helpful suggestions on getting up to speed with Abaqus. Part of this research was performed at the Jet Propulsion Laboratory, California Institute of Technology, under contract with the National Aeronautics and Space Administration.